ACS Sustainable Chemistry & Engineering

Research Article

pubs.acs.org/journal/ascecg

Ecofriendly Route To Synthesize Nanomaterials for Biomedical Applications: Bioactive Polymers on Shape-Controlled Effects of Nanomaterials under Different Reaction Conditions

Vijender Singh,[§] Poonam Khullar,*[,§] Pragnesh N. Dave,[∥] Gurinder Kaur,[‡] and Mandeep Singh Bakshi*[,†]

[†]Department of Chemistry, Wilfrid Laurier University, Science Building, 75 University Ave. W., Waterloo, ON N2L 3C5, Canada

[‡]Nanotechnology Research Laboratory, College of North Atlantic, Labrador City, NL A2 V 2K7, Canada

[§]Department of Chemistry, B.B.K. D.A.V. College for Women, Amritsar 143005, Punjab, India

[∥]Department of Chemistry, Kachchh University, Mundra Road, Bhuj- 370001, Kachchh Gujarat, India

Supporting Information

ABSTRACT: Bioactive diethylaminoethyl dextran chloride (DEAE-D), a versatile polymer with numerous industrial applications, was used as a shape-directing agent for the synthesis of gold (Au) nanoparticles (NPs) in a typical green chemistry synthetic route. Shape-controlled growth was precisely directed by the quaternary amine functionalities of DEAE-D, while its polycationic nature provided simultaneous colloidal stabilization. Mechanistic aspects were drawn from different sets of reactions in which DEAE-D was directly used as a reducing agent with respect to reaction time and temperature. All reactions were simultaneously monitored with UV−visible studies, and NPs were characterized by TEM, SEM, and AFM analysis. Shape-controlled synthesis produced large extraordinarily thin microplates that were converted into small spherical NPs simply by switching the reaction to seed-growth (S-G) mode. DEAE-D-coated NPs thus produced were subjected to hemolysis for their possible use as drug release vehicles in systemic circulation so as to explore their possible biomedical applications.

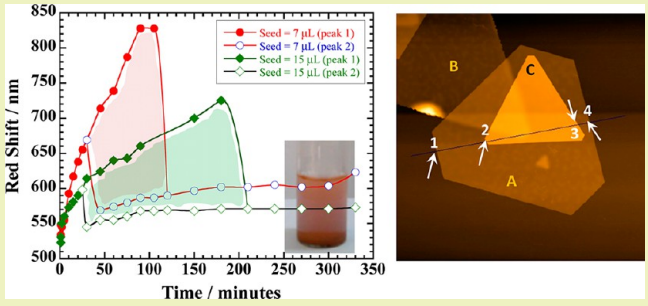

KEYWORDS: *Green chemistry, Biopolymers, Gold nanoparticles, Hemolysis, Reaction mechanism*

INTRODUCTION

Bionanomaterials demonstrate tremendous potential due to their versatile applications in the biomedical field. Synthesis of such materials is usually a several step cumbersome process that needs to tag bioactive molecules to nanomaterials for their appropriate use as biomarkers, drug release vehicles, or cytotoxic agents toward tumor cells. Environmentally friendly green chemistry routes are required to explore their potential use in a wide range of applications. We present the possibility of DEAE-D, a bioactive polycationic derivative of dextran (Figure 1),[1−3] to use for the green chemistry synthesis of bionanomaterials. DEAE-D has high affinity for negatively charged DNA, while its cellulose counterpart is used in ion exchange chromatography and protein and nucleic acid purification as well as separation.[4−6] It is also used as an adjuvant in vaccine production[7,8] and gene therapy,[11] enhances protein and nucleic acid uptake,[9,10] and is used as a protein stabilizer[12] and flocculating agent.[13,14] Its nontoxic nature allows it to be used in oral formulations especially designed to decrease serum cholesterol and triglycerides. These applications primarily relate to its water-soluble nature based on its amphiphilic behavior that arises from a neutral sugar backbone and charged quaternary amine side chains.

Such amphiphiles are excellent shape-directing agents of metal or semiconductor nanoparticles (NPs)[15−17] due to their versatile colloidal stabilizing behavior. The polymer coating of the NPs surface is related to the nature of the polyelectrolyte and is based on its conformational properties due to the polymer architecture and solvent affinity.[18−20] Surface adsorption behavior of the polyelectrolyte is also closely associated with the fundamental aspect of crystal growth of NPs. Generally, the shape and size of NPs are greatly influenced by the effective passivation of different crystal planes of a particular crystal geometry due to the surface coating of a stabilizing agent.[19] A complete passivation of all crystal planes yields a somewhat spherical shape, while the selective coating allows uncoated planes to preferentially participate in the crystal growth to generate a specific shape. For instance, selective adsorption of an amphiphilic molecule on {100} or {110} crystal planes of a face centered cubic (fcc) geometry leads to the formation of rod-shaped structures, and that is quite common in gold (Au) and silver (Ag) NPs, otherwise it generates plate like

Received: May 24, 2013
Revised: August 5, 2013
Published: August 15, 2013

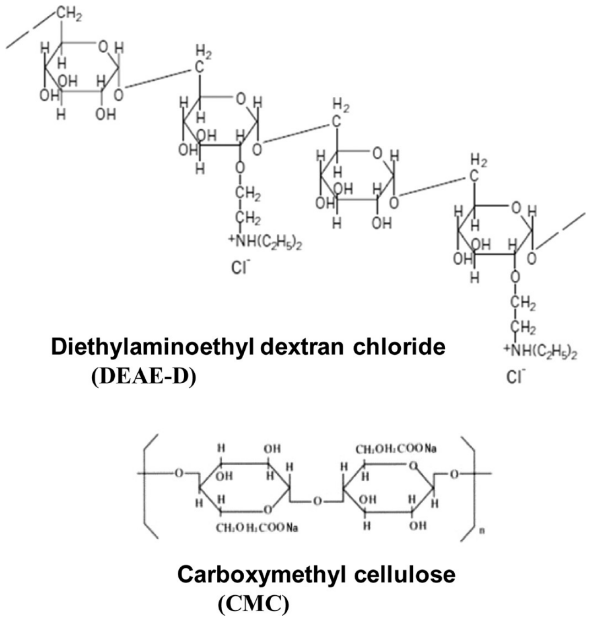

Figure 1. Molecular structures of DEAE-D and CMC.

morphologies.[20−23] Likewise, we expect that DEAE-D also possesses the potential of producing shape-controlled morphologies[24,25] in a typical green chemistry aqueous phase process without using any reducing or stabilizing agents in a single step reaction. Although numerous reports[15−25] are available in the literature on the shape-controlled effects of small amphiphilic molecules such as surfactants and other water-soluble neutral species, mechanistic aspects related to the stepwise growth kinetics of bionanomaterials especially by using a bioactive polymeric species are rarely attempted.[16,17] Thus, DEAE-D is considered to be an important candidate for a shape-controlled green chemistry synthesis of bionanomaterials with potential applications in bionanotechnology.

The choice of DEAE-D is based on two aspects: its mild reducing behavior to reduce Au(III) into Au(0) due to the presence of ether oxygens in the sugar backbone[16,17] and its polycationic nature that attracts negatively charged gold ions ($AuCl_4^-$) and makes them available for ether oxygens to initiate the reduction reaction. Both aspects further depend on the aggregation behavior of DEAE-D that is greatly influenced by the temperature variation. Thus, a direct insight into the physiochemical aspects of DEAE-D and their influence on the nucleation and shape-controlled effects is the key to elucidate the mechanistic aspects and growth kinetics of nanomaterials. To elaborate it further, we compare DEAE-D behavior with that of its anionic cellulose derivative counterpart, carboxymethyl cellulose (CMC) (Figure 1), which also possesses a similar reducing ability to convert Au(III) into Au(0) but lacks quaternary amine side chains. CMC is another well-known water-soluble bioactive polymer with several important applications such as use a viscosity modifier, emulsion stabilizer, lubricant, etc. It is also used as a stabilizing agent in the synthesis of Au NPs.[26] A comparison between the behaviors of DEAE-D and CMC allows us to have a direct insight into the crystal growth of Au NPs on the basis of their respective cationic and anionic natures as well as the presence and absence of quaternary amine functionalities. DEAE-D-coated NPs thus synthesized have been employed for the hemolysis assay to explore their potential as drug release vehicles in systemic circulation in view of the remarkable uses of DEAE-D as an adjuvant in vaccine production[7,8] and gene therapy[11] and as a protein stabilizer.[12]

EXPERIMENTAL SECTION

Materials. Chloroauric acid ($HAuCl_4$), diethylaminoethyl dextran chloride (DEAE-D), white powder, average molar mass = 500,000, hygroscopic, lot # 39 H1323, and carboxymethyl cellulose sodium salt (CMC), white powder, n = 500 (Figure 1) were purchased from Sigma-Alrdich. Double distilled water was used for all preparations.

Synthesis of Au NPs. Two methods were adopted for the synthesis of Au NPs: direct reduction method by polymer and seed-growth (S-G) method.

Direct Reduction Method. Aqueous mixtures (total 10 mL) of DEAE-D or CMC and $HAuCl_4$ (0.25−1 mM) were taken in screw-capped glass bottles. After mixing the components at room temperature, the reaction mixtures were kept in a water thermostat bath (Julabo F25) at the precise temperature of 70 ± 0.1 °C for 6 h under static conditions. In the case of DEAE-D, within 15−30 min of the reaction, the color of the solution started changing from colorless to pink and thereafter shiny large colloidal NPs started settling at the bottom of the tube in high yield. After 6 h, almost all particles settled at the bottom with a golden-yellow color (Figure S1, Supporting Information). However, in the presence of CMC, no large NPs settled at the bottom, but rather bright colored suspensions were obtained with color ranging from dark pink to brown gray (Figure S2, Supporting Information).

S-G Method. First, 25 mL of seed solution was prepared by boiling an aqueous mixture of 1 mM $HAuCl_4$ and 3.5 mM Na_3Cit. Growth solution was prepared in screw-capped glass bottles by mixing a small quantity of seed solution (7−50 μL) with an aqueous mixture of DEAE-D and $HAuCl_4$ (0.25−1 mM) in a total volume of 3 mL. After mixing the components at room temperature, the reaction mixtures were kept in a water thermostat bath (Julabo F25) at the precise temperature of 70 ± 0.1 °C for 6 h under static conditions. The final color of each solution was pink or purple.

The samples were cooled to room temperature and kept overnight. They were purified with pure water at least three times in order to remove unreacted polymer. Purification was done by collecting the Au NPs at 8000−10,000 rpm for 5 min after washing each time with distilled water.

Methods. The progress of each reaction was monitored by simultaneous UV−visible measurements within the temperature range of 20−70 °C as well as reaction time to determine the absorbance due to surface plasmon resonance (SPR) of Au NPs. All reactions were performed in the UV cuvette of a Shimadzu-Model No-2450 (double beam). This instrument is equipped with a TCC 240A thermoelectrically temperature controlled cell holder that allows for measuring the spectrum at a constant temperature within ±1 °C.

Transmission electron microscopic (TEM) analysis was done on a JEOL 2010F at an operating voltage of 200 kV. The samples were prepared by mounting a drop of a solution on a carbon-coated Cu grid and allowing to dry in air. Scanning electron microscopic (SEM) analysis was carried out on a Zeiss NVision 40 Dual Beam FIB/SEM instrument. Photomicrographs were obtained in bright field scanning/imaging mode, using a spot size of ∼1 nm and 12 cm of a camera length. Energy dispersive X-ray spectroscopic (EDS) microanalysis was carried out using an Oxford INCA atmospheric ultrathin window (UTW), and the data were processed using the Oxford INCA Microanalysis Suite Version 4.04. Atomic force microscopic (AFM) measurements were carried out using a model Veeco diCaliber at room temperature. A total of 25 μL of a purified aqueous suspension of gold colloids was drop coated on an ultra-cleaned glass coverslip and left to dry in a drybox. It was then scanned with silicon nitride tips in contact mode to get amplitude and height images. The survey scanned images were processed and analyzed by using SPM graphic software to obtain three-dimensional topography of large Au NPs.

X-ray diffraction (XRD) patterns were recorded by using a Bruker-AXS D8-GADDS with T_{sec} = 480. Samples were prepared on glass

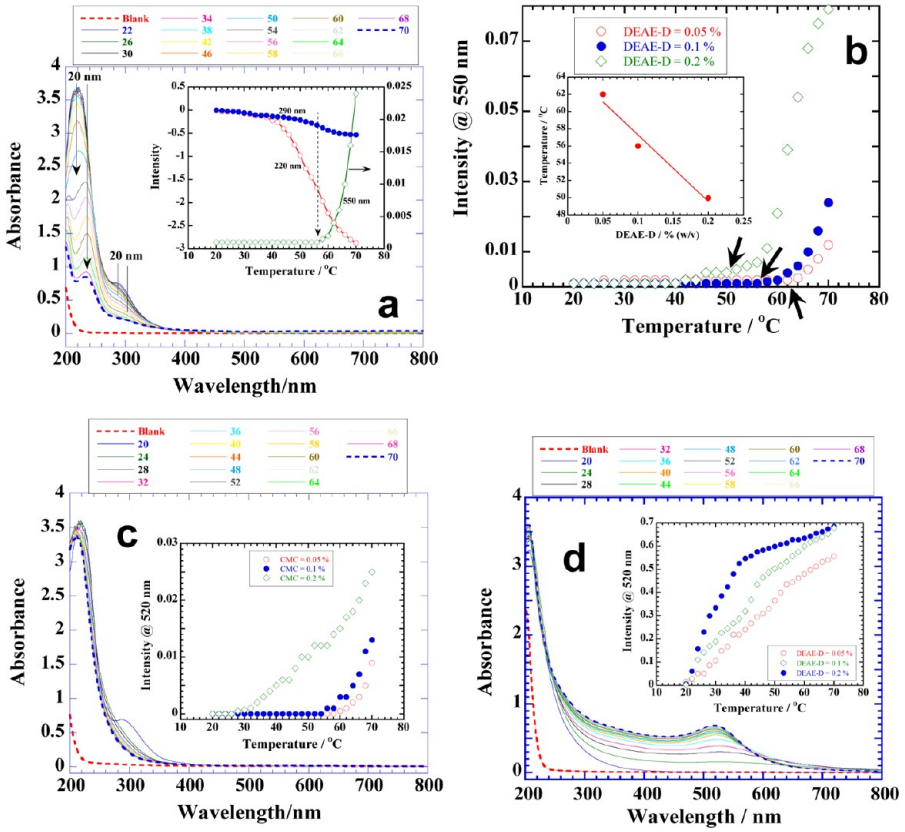

Figure 2. (a) Typical example of a reaction in aqueous phase of 0.1% DEAE-D and 0.25 mM $HAuCl_4$ under the effect of temperature variation from 20−70 °C and simultaneously monitored by the UV−visible measurements. Red dotted line refers to blank (i.e., aqueous 0.1% DEAE-D without gold salt), and blue dotted line represents the scan at 70 °C. Scans from top to bottom follow the 20−70 °C temperature range. Inset shows the variation in the normalized intensity of different peaks with temperature. (b) Variation of intensity of 540 nm peak versus temperature for the same reaction at different DEAE-D concentrations. The inset depicts the linear variation in the reduction temperature (indicated by the black arrows for each reaction) with the amount of DEAE-D. (c) UV−visible scans of a reaction of 0.1% CMC and 0.25 mM $HAuCl_4$ under the effect of temperature variation from 20−70 °C. Red dotted line refers to blank (i.e., aqueous 0.1% CMC without gold salt), and blue dotted line represents the scan at 70 °C. Scans from top to bottom follow the 20−70 °C temperature range. Inset shows the variation of intensity of the 520 nm peak with temperature of the same reaction at different CMC concentrations. (d) UV−visible scans of the reaction of (a) at pH 9.5 depict the effect of pH. Inset shows the intensity variation of the 520 nm peak with temperature at pH 9.5 with different amounts of DEAE-D. Intensity of the 520 nm peak increases from 20−70 °C. See details in the text.

slides by placing a concentrated drop of aqueous suspension and then drying in a vacuum desiccator.

RESULTS

Direct Reduction Method. *Temperature Effect.* Aqueous solutions of both DEAE-D and CMC do not show any absorbance in the UV or visible region within 20−70 °C (Figure 2a, dotted line; Figure S3, Supporting Information). However, in the presence of $HAuCl_4$ along with DEAE-D (Figure 2a), two prominent peaks are observed around 220 and 290 nm in the UV region along with a very weak and much broader band around 550 nm in the visible region (magnified in Figure S4, Supporting Information) due to $AuCl_4^-$ ions, ligand to metal charge transfer (LMCT) between the gold ions and polymer as observed previously for similar reactions with block polymers,[27−29] and SPR of NPs, respectively.[16,17] Their normalized intensity variation is depicted in the inset of Figure 2a, where first two peaks show a regular decrease with an increase in temperature along with a red shift of 20 nm, whereas the third peak shows a regular increase. A close inspection of this figure indicates that the absorbance of Au NPs due to SPR resonance (550 nm) starts becoming prominent around 56 °C, and the LMCT complex (290 nm) also starts converting into nucleating centers around this temperature, which is indicated by a slight decrease in the 290 nm peak. This happens when the $AuCl_4^-$ ions complex with oppositely charged DEAE-D as DEAE-D aggregates dismantle with temperature from 40 to 56 °C, and hence, the 220 nm peak shows a steep fall. At 56 °C, the LMCT complex (290 nm) attains sufficient energy to convert into nucleating centers and thus leads to the formation of Au NPs.[16,17] This temperature (reduction temperature, indicated by black arrows, Figure 2b) decreases linearly with an increase in the amount of DEAE-D, which means that the reduction of Au(III) into Au(0) through Au(I) represented by the LMCT complex is proportional to the amount of DEAE-D. A 20 nm red shift in both peaks (i.e., 220 and 290 nm, Figure 2a) indicates the ongoing conformational changes in DEAE-D under the effect of temperature. As α-1,6 glycosidic linkages between glucose molecules constitute the backbone of DEAE-D (Figure 1), inter- as well as intra-hydrogen bonding is expected to cause aggregation at low temperature, which might restrict the approach of $AuCl_4^-$ ions to electron-donating ether oxygens. Dismantling of the aggregates with temperature allows the $AuCl_4^-$ ions greater access for electron-donating sites to facilitate electron transitions from predominantly ligand $3e_u(\pi)$ to metal $3b_{1g}(\sigma^*)$.[16] That in turn decreases the energy difference

between the ligand and metal molecular orbitals and hence shifts the LMCT band to lower energy with a red shift of 20 nm.

Although peaks at 220, 290, and 520 nm due to $AuCl_4^-$ ions, LMCT, and SPR of NPs, respectively, are observed in the case of CMC (Figure 2c), no marked decrease in the intensity of the 220 nm band is observed with temperature. Also, LMCT (290 nm) vanishes almost instantaneously in the beginning of the reaction, which provides a greater reduction potential to CMC with the consequence of 0.2% CMC initiating the reduction at a relatively much lower temperature (~ 30 °C) than 0.2% DEAE-D (~ 50 °C, Figure 2b) under identical reaction conditions. However, the growth rate is faster with a greater slope for 0.2% DEAE-D rather than CMC, which means larger morphologies are expected in the former case. The absence of quaternary amine groups in CMC is responsible for the formation of no stable LMCT complex, and that is why $AuCl_4^-$ ions instantaneously convert into nucleating centers as soon as they come in contact with the ether oxygens. In order to authenticate this proposed mechanism, we conducted the reaction for DEAE-D at pH 9.5 (Figure 2d), which reduces the possibility of electrostatic interactions between the quaternary amine groups and $AuCl_4^-$ ions to generate a stable LMCT complex. Remarkably, high pH has completely removed the peak due to the LMCT complex generating a much more prominent peak due to SPR at 520 nm, the variation of which is depicted in the inset. Thus, high pH allows DEAE-D to initiate the reduction even at 20 °C or as soon as the $AuCl_4^-$ ions come in contact because they are no longer entrapped by the quaternary amine groups to generate the LMCT complex. Thus, a significant difference in the reduction mechanisms of DEAE-D and CMC is expected to have a marked effect on the crystal growth of Au NPs in the presence of respective polymers (which will be further discussed in the microscopic analysis section).

Time Effect. UV−visible scans of a typical reaction of DEAE-D at a constant 70 °C with reaction time (Figure 3a) also show prominent peaks at 220, 290, and 550 nm due to $AuCl_4^-$ ions, LMCT, and SPR of NPs, respectively, as noted previously. Variation in the intensity of all peaks with time is depicted in Figure 3b and c, for 0.25 and 1 mM $HAuCl_4$, respectively. In the former case, the reduction is completed within 50 min of the reaction. Within this period (close up view, inset), the intensity of $AuCl_4^-$ ions (220 nm) and LMCT (290 nm) decreases continuously due to the formation of tiny nucleating centers with insignificant absorbance at 550 nm up to 15 min (see dotted line). Thereafter, both the 220 and 290 nm peaks disappear because fresh $AuCl_4^-$ ions engage themselves in the autocatalytic reduction[30−32] on the already created nucleating centers without going through LMCT, which causes an increase in the absorbance of Au NPs. As this process continues, NPs eventually grow into extraordinarily large sizes and settle at the bottom of the tube (see Experimental Section and Figure S1, Supporting Information) leaving a constant absorbance of Au NPs in aqueous phase.

On the other hand, when the concentration of gold salt is increased to 1 mM, the same reaction takes about 330 min (more than 4-fold increase) to complete (Figure 3c). Interestingly, a similar variation in the intensity of all peaks (except $AuCl_4^-$ ions) is observed within 15 min (see inset) because the same amount of DEAE-D is used with essentially same number of available ether oxygens to create the nucleating centers. However, a greater amount of gold salt does not allow the intensity of $AuCl_4^-$ ions (220 nm) to decrease even up to 100 min of the reaction due to a limited number of available ether oxygens. That is why LMCT still exists (even after 15 min) as more than one $AuCl_4^-$ ion is expected to form the LMCT complex with each reducing site as is evident from the low energy absorbance (310 nm, Figure S5, Supporting Information) in comparison to relatively high energy absorbance (290 nm) obtained for 0.25 mM $HAuCl_4$ (Figure 3a). Importantly, intensity of both 220 and 310 nm peaks continuously decreases until 330 min, whereas that of Au NPs tends to remain constant just after 15 min (like that of Figure 3b). This means that the number density of suspended colloidal NPs practically remains constant in this reaction too after 15 min, while the excess amount of $AuCl_4^-$ ions involved in the autocatalytic process continuously replaces them with large shiny NPs that settle at the bottom of the tube (see Experimental Section and Figure S1, Supporting Information).

In the case of CMC, time effect does not produce any LMCT band (Figure S6, Supporting Information) as observed for temperature effect (Figure 2c), while a clear absorbance due to SPR of Au NPs around 520 nm is observed (Figure 3d). It remains quite weak up to 100 min; thereafter, it increases with a red shift of about 50 nm and bifurcates to produce an even much stronger absorbance at longer wavelength of 850 nm. This variation has been depicted in Figure 4e and divided into three parts especially for a reaction of 1 mM $HAuCl_4$. Weak absorbance in the first part can be attributed to the presence of tiny NPs which may coalesce in the second part as indicated by a red shift of 50 nm, and then produce large NPs or arrange themselves in nanowires with prominent absorbance at 850 nm. Usually, rod or nanowires produce simultaneously two absorbances; one at shorter wavelength (520 nm) is due to the short axis (traversed SPR) and other at longer wavelength (850 nm) is due to the long axis (longitudinal SPR, depends on the length). Reaction with 0.25 mM $HAuCl_4$ does not show this behavior and growth process tends to constant after sometime. Thus, a comparison between the results of Figure 3b and c with that of Figure 3d and e indicates that DEAE-D has a precise control over the growth kinetics of Au NPs while this is not so when CMC is used because the profiles of growth kinetics of Figure 3e of different gold salt concentrations indicate the formation of different morphologies.

S-G Method (Temperature Effect). In this reaction protocol, we want to direct the growth on already present seeds in the solution to develop shape-controlled morphologies. Figure 4a and b show two UV−visible scans of reactions conducted with a constant amount of 7 μL of the Au seed solution along with 0.25 and 1 mM $HAuCl_4$, respectively, in the presence of DEAE-D. In both cases, broad absorbance of Au NPs is initially located around 540 nm, which increases with an increase in temperature and also red shifts (indicated by the arrows). We call this as peak 1. It gets broader in Figure 4a but splits into two in Figure 4b to produce another peak (peak 2) at a lower wavelength. A much greater amount of $HAuCl_4$ (1 mM) in the latter case in comparison to the former (0.25 mM) causes a shape transformation and is responsible for the appearance of peak 2 because a 4-fold higher amount of gold atoms are now accommodated on a constant amount of seed (i.e., 7 μL). A variation in the wavelength of both peaks (i.e., peak 1 and peak 2 of Figure 4b) is depicted in Figure 4c where filled circles (for 7 μL) show a huge red shift of ~180 nm in peak 1, which bifurcates to produce peak 2 (empty circles) around 55 °C. The shaded area refers to the region where two peaks coexist. Almost double the amount of seed (15 μL, diamonds) reduces

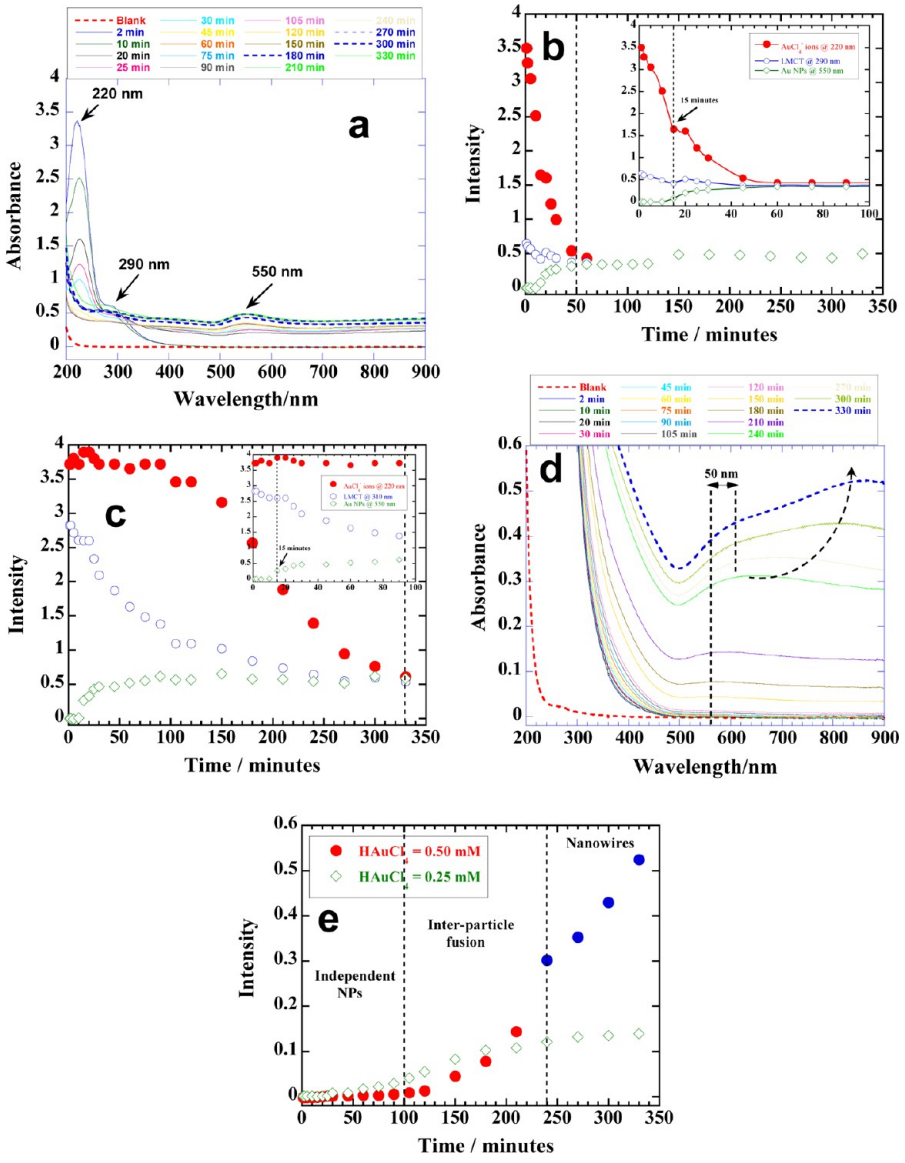

Figure 3. (a) Typical example of a reaction in aqueous phase of a reaction of 0.05% DEAE-D and 0.25 mM $HAuCl_4$ with time depicting absorbances at 220, 290, and 550 nm. (b) Variation in the intensity of these absorbances with time for a reaction with 0.25 mM and (c) 1 mM $HAuCl_4$. (d) Plots of a similar reaction with time for 0.05% CMC and 0.5 mM $HAuCl_4$ demonstrating only broad absorbances. (e) Variation in the intensity of broad absorbance around 550 nm that increases and red shifts with reaction time. Two different curves represent two reactions of 0.05% CMC with 0.25 and 0.5 mM $HAuCl_4$. Red and blue filled circles belong to the same reaction and represent different regions. See details in the text.

the red shift to ~100 nm and produces peak 2 at an even higher temperature of 66 °C, while 50 μL of the seed (triangles) further reduces the red shift to just 40 nm without the appearance of peak 2. This sequence points to the fact that the entire growth process is precisely controlled and directed by DEAE-D to happen only on the existing number of seeds. That is why the shape transformation vanishes with an increasing amount of seed.

S-G Method (Time Effect). The same reactions when conducted at a constant 70 °C with time produce a similar variation in the wavelength of Au NPs absorbance (Figure 4d). Absorbance appears around 540 nm (peak 1) and demonstrates a continuous red shift with time. Within 50 min of the reaction, it bifurcates to generate peak 2 at a lower wavelength (as noticed in Figure 4c), which ultimately survives while peak 1 disappears. The only difference between the two reactions is that one can see a large red shift of ~300 nm when 7 μL of the seed is used in comparison to ~200 nm for 15 μL of seed due to a greater growth in the former case that leads to the formation of much larger morphologies. The time period in respective reactions where two peaks coexist, i.e., the respective shaded area of the phase diagram, in fact represents the growth kinetics of shape transition in growing NPs. This means that in the beginning of the reaction (i.e., before the shaded area) peak 1 produces only one kind of shape that continuously grows with a prominent red shift, while within 50 min of the reaction another shape appears that absorbs at a shorter wavelength and is represented by peak 2. Meanwhile the reaction mixture also shows the presence of two kinds of particles. Large orange colored particles settled at the bottom, while smaller ones were in suspension (inset). Peak 1 in fact belongs to large particles that settle at the bottom and hence disappear as particles grow to certain size and cannot support themselves in colloidal suspension. The reaction completes when peak 1 disappears because

dx.doi.org/10.1021/sc400159x | ACS Sustainable Chem. Eng. 2013, 1, 1417−1431

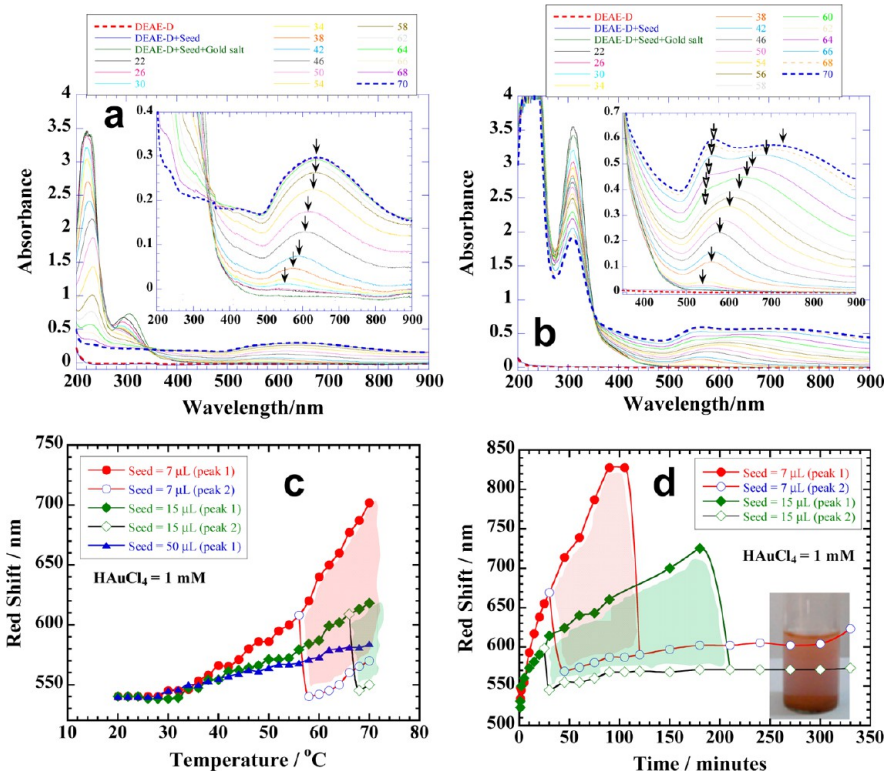

Figure 4. Typical examples of seed-growth reactions in an aqueous phase of 0.05% DEAE-D and 7 μL of seed solution with (a) 0.25 mM and (b) 1 mM $HAuCl_4$ under the effect of temperature variation from 20−70 °C. Insets in both figures show the magnified view of 540 nm peak, which red shifts with an increase in temperature and is indicated by the solid arrows. This peak is termed as "peak 1", while another peak produced in (b) is indicated by the empty arrows and is termed "peak 2". (c,d) Variation in the wavelegth of these peaks with temperature and time, respectively, by using different amounts of seed solution. See details in the text.

peak 2 remains more or less constant with time. Thus, Figure 4c and d are complementary figures of the same reactions with temperature and time, respectively, and again demonstrates a precise control of DEAE-D on the growth of Au NPs because the reaction is precisely directed on the number of available seeds in the solution. Whereas, this is not the case with CMC (Figure S7, Supporting Information) where we do not see any substantial growth in seeds and behavior is more or less the same as is depicted in Figure 2c and 3d, which means that CMC is not directing the growth on already available seeds as DEAE-D can do.

Microscopic Studies. *Au NPs–DEAE-D Samples.* Microscopic studies help us to understand the difference in the reduction and stabilizing behaviors of DEAE-D and CMC that altogether results in different shapes and structures of Au NPs. The presence of DEAE-D produces several micrometer-sized triangular and hexagonal thin plates[33,34] (Figure 5a) carrying aggregates of small faceted Au NPs (Figure 5b) in all samples. Some of the microplates even reach the size of 20 μm with average sizes varying between 5 and 15 μm, which is huge in comparison to that of NPs (~150 nm). EDX analysis of NPs (Figure 5c) shows the maximum amount of Au followed by C, Cl, and O coming from the DEAE-D coating. The golden-yellow shiny particles settled at the bottom of sample tubes (Figure S1, Supporting Information) are in fact large microplates. They start settling at the bottom of the tube after 15 min of the reaction according to Figure 3b and c because thereafter the absorbance of colloidal Au NPs (shown in Figure 5b) in the solution becomes constant. These microplates seem to generate from the merger of the smaller ones.[35] Figure 5d provides direct evidence where one can see a single large somewhat hexagonal plate being derived from smaller ones whose merged boundaries are still visible (indicated by the white arrows). Similarly Figure 5e shows another image of a large plate undergoing the same process along with the presence of other smaller plates with wavy margins (indicated by empty block arrows) ready to merge to produce larger plates. This information is further substantiated with TEM images (Figure S8, Supporting Information). EDS analysis of the single plates confirms the presence of Au (Figure 5f) along with the DEAE-D coating. A TEM image of a single hexagonal microplate is shown in Figure 5g along with the corresponding SAED pattern (Figure 5h) of hexagonal symmetry indicating the fact that the microplate is a single crystal with preferential growth along the {111} crystal planes of fcc geometry, which is also supplemented by the corresponding XRD patterns with a single prominent peak at 38.2° (Figure 5i). An increase in the amount of gold salt from 0.25 to 1 mM converts some plates into large sheets (Figure 5j) as demonstrated by Figure 3c over a time period of 330 min. Each sheet bears surface patterns originating from the regular interference fringes and the bending contours produced by its extraordinary thin nature.[35,36]

We get similar thin microplates (Figure 6a−c) carrying faceted NPs (Figure 6d) when we increase the amount of DEAE-D from 0.05% to 0.1%. But further a increase in the amount up to 0.2% generates more NPs and places them in large quantities on the microplates (Figure 6e,f). Some of the plates are completely loaded with NPs and nanorods (Figure 6g) that are stacked together in an ordered fashion (Figure 6h). A sideways as well as end-to-end stacking of the nanorods indicates

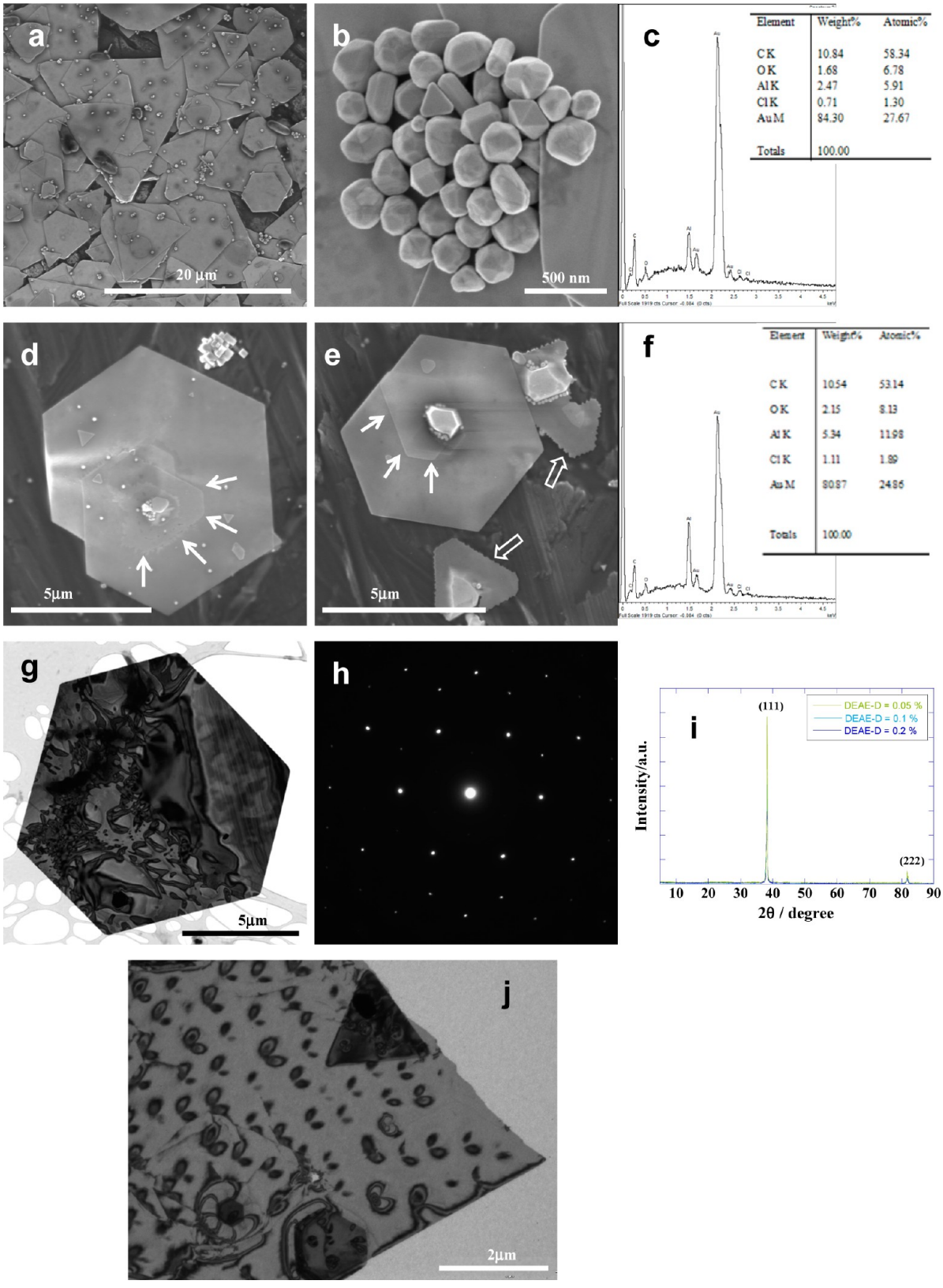

Figure 5. (a) SEM image of several microplates carrying groups of small Au NPs synthesized with 0.05% DEAE-D and 0.25 mM $HAuCl_4$ at 70 °C. (b) Close-up image of a group of faceted Au NPs and (c) its corresponding EDS analysis. (d,e) Images of single large hexagonal plates made from the merger of smaller ones through their lateral planes shown by the white arrows. (f) Corresponding EDS analysis of a single plate. (g) TEM image of another single plate and (h) its corresponding selected area electron diffraction pattern (SAED). (i) XRD patterns of the samples prepared with different amounts of DEAE-D. (j) TEM image of a large Au sheet. See details in text.

dx.doi.org/10.1021/sc400159x | *ACS Sustainable Chem. Eng.* 2013, 1, 1417−1431

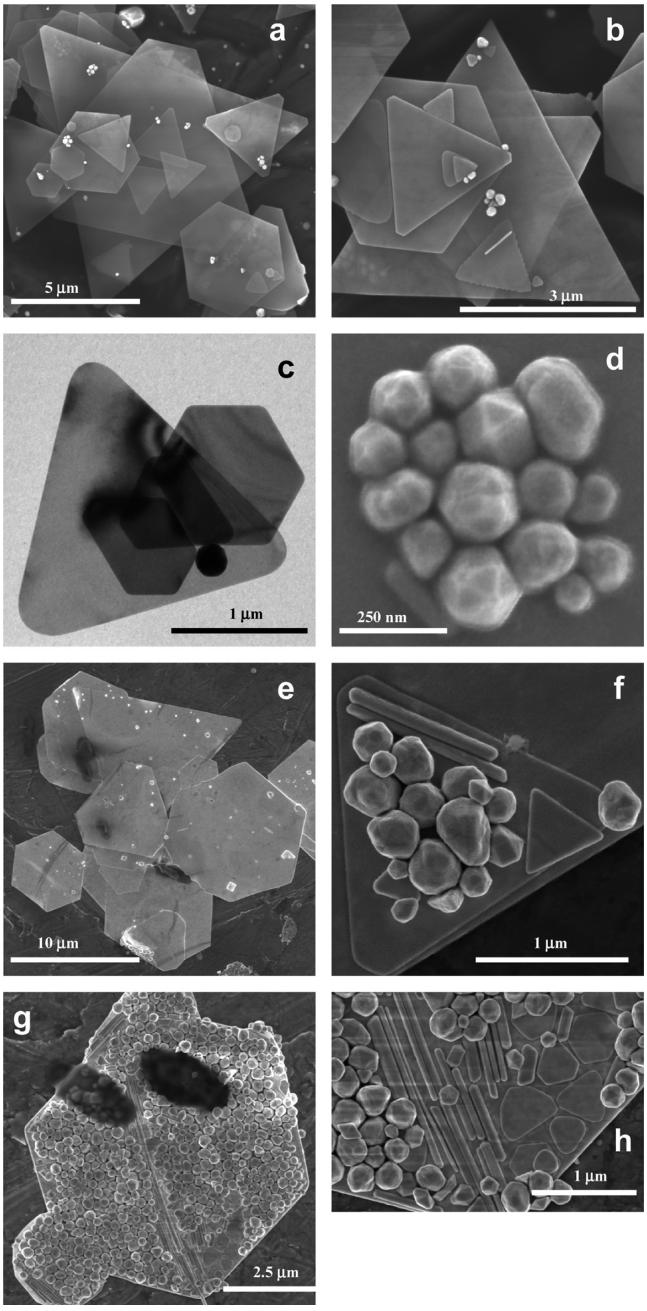

Figure 6. (a,b) SEM and (c) TEM images of several thin microplates stacked one above the other synthesized with 0.1% DEAE-D and 0.25 mM $HAuCl_4$ at 70 °C. (d) Group of faceted NPs of the same sample. (e) SEM image of the sample prepared with 0.2% DEAE-D and 0.25 mM $HAuCl_4$ at 70 °C. (f–h) Images of self-assembled NPs of different shapes on large microplates. See details in text.

that DEAE-D apart from stabilizing the NPs by surface coating also helps in their self-aggregation. DEAE-D is well-known flocculating agent[13,14,37−40] that helps in the self-aggregation of colloidal particles. This is not expected during the drying process of the samples for the TEM or SEM studies because we see no reason why a huge number of small NPs would prefer to accommodate on a single microplate as shown in Figure 6f and g rather lying scattered in the sample. Thus, these figures are the best examples of accommodation of NPs of different shapes on large microplates due to the flocculating behavior of DEAE-D, which can be explained on the basis of the DLVO theory[41,42] as reported elsewhere.[43,44] Adsorption of DEAE-D on the NP surface is expected to take place through the quaternary amine head groups[45] just like that of cetyltrimethyl ammonium bromide (CTAB),[25,46−48] a well-known stabilizer and shape-directing agent. This leaves a sugar backbone in the aqueous phase for hydrogen bonding with similar moieties from other NPs (Figure 7a). Hence, hydrogen bonding seems to be the driving force for the flocculating behavior of DEAE-D coated NPs and their accommodation on large microplates. One can clearly see the glue-type DEAE-D coating responsible for the self-aggregation of NPs in Figure 7b (indicated by white

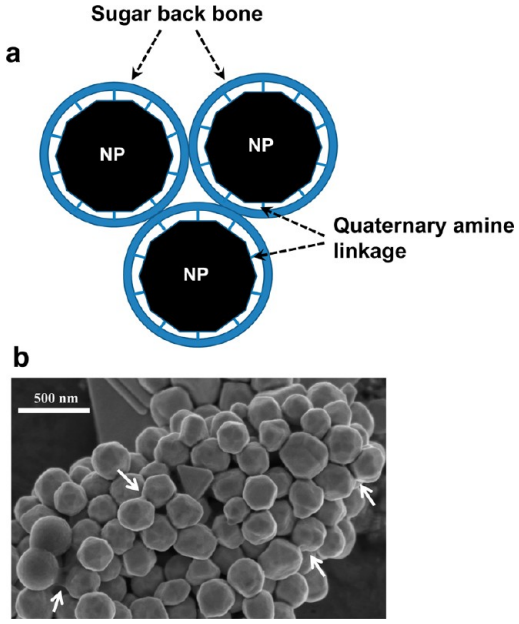

Figure 7. (a) Schematic representation of DEAE-D capped Au NPs. (b) Self-aggregated faceted Au NPs due to DEAE-D capping. See details in text.

arrows). Interestingly, if we drastically increase the amount of DEAE-D from 0.2% to 0.8%, we get fine core–shell morphologies with a single NP forming the core and a thick coating of DEAE-D constituting the shell (Figure 8). The thickness of the shell remains constant around ∼75 nm though the size of the NP decreases from ∼450 nm (Figure 8a) to ∼75 nm (Figure 8d), which indicates that the coating is DEAE-D concentration specific because when the amount of DEAE-D is 0.2% the thickness of the coating is hardly visible (Figure 7b). This thick coating in the form of a shell suggests a high degree of association among the capping layers of DEAE-D. A decrease in the size of Au NP likewise probably indicates a greater shape control of an increasing amount of DEAE-D.

Microplate Thickness Measurements. AFM studies help us in quantification of the thickness of the microplates and size distribution of NPs. Figure 9a and b shows the deflection and height images of two microplates. Thickness of the plates was measured by performing the line analysis on both plates separately. A blue line passing through plate "A" allows us to determine the thickness of this plate from points "1" and "2". The corresponding scan is illustrated in the upper frame of Figure 9c along with the thickness in adjoining table. Both points measure the thickness around 47 nm, which suggets a fairly flat plate. Likewise, a red line passing through plate "B" gives an average thickness of 45 nm. Figure 9d shows another

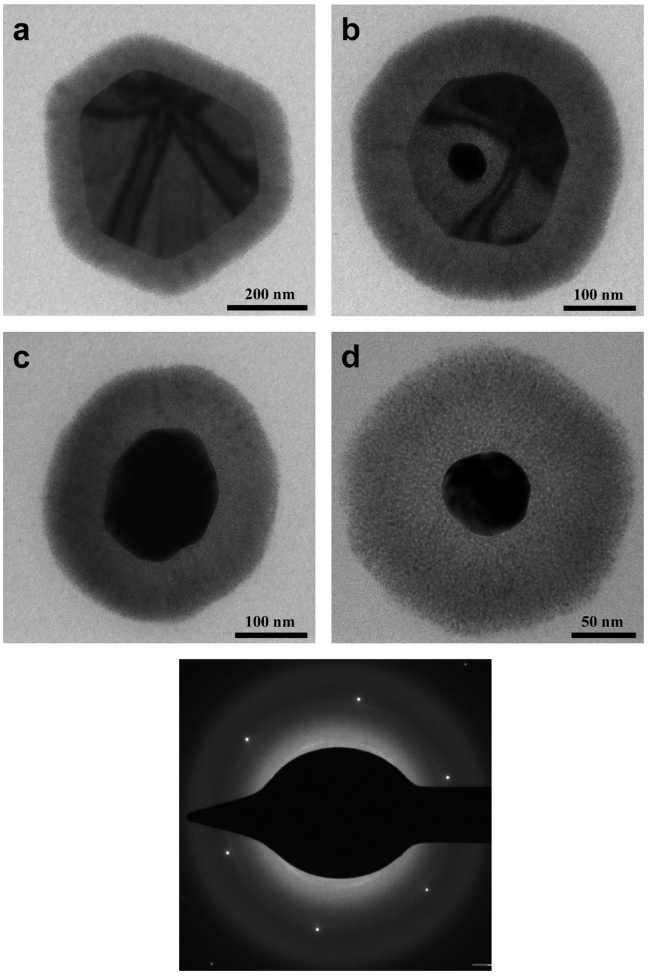

Figure 8. (a–d) TEM images of a single Au NP coated with a thick layer of DEAE-D in a typical core–shell morphology prepared with 0.2–0.8% DEAE-D and 0.25 mM $HAuCl_4$ at 70 °C and (e) its corresponding SAED pattern. No staining agent has been used. See details in text.

image of two plates lying one above the other. Line analysis simultaneously measures the thickness of both plates. Points "1" and "4" allow us to measure the thickness of the lower larger plate, which is about 41 nm, but the thickness of the upper triangular plate (points "2" and "3") is 80 nm, which is almost double than that of the lower one. These microplates are quite thin in comparison to those already reported in the literature.[33,34,45,49]

Figure 9f and g shows self-assembled NPs on the microplates as previously depicted in TEM images (Figure 6f,g). Line analysis (Figure 9h) measures the average size of NP close to 154 nm, which is in good agreement with that of TEM analysis (Figure 5b). An increase in the amount of DX to 1.6% produces very large plates of about 30 μm in size. One such large plate is shown in Figure 9i with interesting features that are not demonstrated by other images. This plate has a large variation in thickness, and the line scan is presented in Figure 9j along with the thickness data in the adjoining table. The left edge of the plate provides a thickness close to 1 μm, which continuously decreases toward the opposite edge (see thickness data in the table), and the final thickness of most of the plate is 38 nm, which is close to that for plates from the previous images. It seems that as if the left vertex (indicated by an arrow) of this hexagon is further involved in the growth process, and the growth spans slowly to cover rest of the plate resulting in a much thicker plate similar to the one shown in Figure 9f and g bearing large NPs. This is basically triggered by the active sites on the lattice plane that are created by the dislocation and imperfections in the atomic arrangement and are usually prevalent on the vertices, edges, or grain boundaries as previously shown in Figure 5d and e. Usually, a typical crystallization process proceeds through a layer-by-layer growth with an approximate thickness of 1 nm. This is carried out by freshly produced atomic species or nucleating centers in the solution, which approach the surface and look for the active sites with greater surface energy over rest of the crystal planes. The active sites then attract them favorably and allow them to integrate into the lattice plane. Figure 9i shows this process clearly as it proceeds from left to right in a typical layer-by-layer fashion, and that is why the thickness decreases from 1043 to 38 nm as growth proceeds from left to right. Because the growth process is spanning over an area of several micrometers, some of the imperfections survive during the growth process and lead to the formation of large NPs. On the contrary, if there are little imperfections as in the case of large plate shown in Figure 9a, b, d, and k, the thickness remains the same throughout the microplate (note the average thickness of ~54 nm, Figure 9l). The presence of surface wrinkles on the plate of Figure 9k is mainly caused by the extraordinarily thin nature in comparison to a surface area of several micrometers.

Au NPs–CMC Samples. CMC on the other hand produces entirely different morphologies from that of DEAE-D as indicated by the UV–visible behavior (Figure 3d,e). No microplate formation happens in the presence of CMC (Figure 10a), and instead Au NPs of polyhedral shapes of 43 ± 9 nm are produced, which are arranged in chain-like arrangements due to the CMC coating. As the amount of gold salt increases from 0.25 to 0.5 mM, it converts the chain-like arrangement into continuous nanowires of ~10 nm thick (Figure 10b,c). Polyhedral morphologies are usually bound with high energy {111} crystal planes. An increase in the amount of gold salt preferentially involves them in the growth process to convert the chain-like arrangement into continuous nanowires, which is facilitated by the CMC coating. XRD patterns (Figure 10d) further support this inference where one can find a single prominent peak at 38.2° representing the substantial growth along the {111} crystal planes of fcc Au. Similar behavior is reported for phospholipid-stabilized Au NPs.[50]

The morphologies of the Au NPs generated by the S-G method are not much different from that we have discussed above. The S-G method clearly depicts the formation two kinds of morphologies for reactions with DEAE-D from UV–visible behavior (Figure 4c,d), which are fully supported by the TEM images (Figure S9, Supporting Information). Small NPs represented by peak 2 of Figure 4c and d and large microplates represented by peak 1 (because plates grow and then settle at the bottom) with both 7 and 15 μL of the seed solution are shown in Figure S9a,b and c,d of the Supporting Information, respectively. However, plate formation can be dramatically reduced if 50 μL of the seed solution is used, which generates fine spherical NPs (Figure S9e, Supporting Information). This happens because the fixed amount of gold salt is distributed over a large number of seeds and does not get a chance to grow into microplates. In contrast, CMC still produces polyhedral morphologies (Figure S10, Supporting Information) even in the presence of seeds with no sign of shape-controlled growth

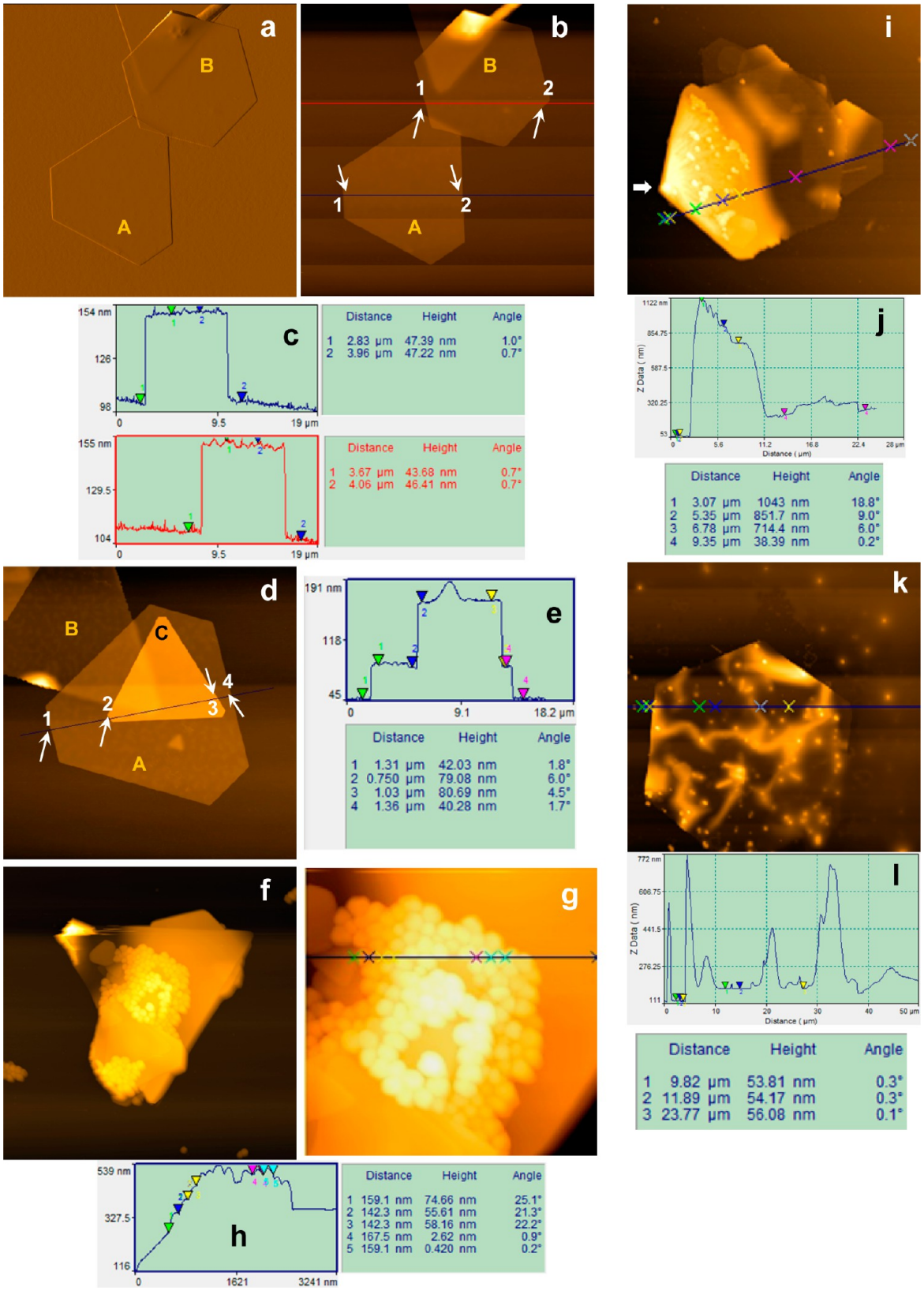

Figure 9. (a,b) AFM deflection and height images, respectively, of two microplates prepared with 0.05% DEAE-D and 0.25 mM $HAuCl_4$ at 70 °C. (c) Line analysis to determine the thickness of both plates. Upper frame gives the line analysis of plate "A", and lower frame provides the line analysis of plate "B". (d) Height image of few microplates lying one above the other and (e) its corresponding line analysis. (f) Height image of self-assembled NPs on a triangular microplate prepared with 0.1% DEAE-D and 0.25 mM $HAuCl_4$ at 70 °C and (g) its close up image with line analysis given in (h). (i) Height image of a large microplate prepared with 1.6% DEAE-D and 0.25 mM $HAuCl_4$ at 70 °C. (j) Line scan demonstrates the variation in the thickness of this plate from left to right. (k) Height image of a large plate with a wrinkled surface but of a constant thickness of ∼54 nm as depicted by (l) line scan. See details in text.

dx.doi.org/10.1021/sc400159x | *ACS Sustainable Chem. Eng.* 2013, 1, 1417−1431

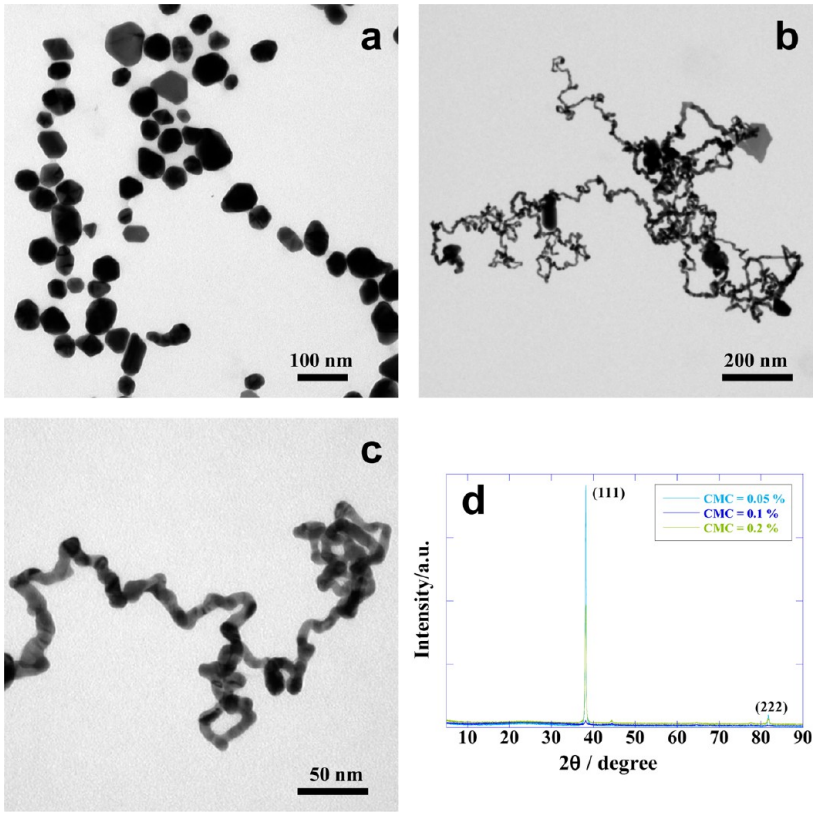

Figure 10. (a) TEM image of polyhedral Au NPs prepared with 0.05% CMC and 0.25 mM $HAuCl_4$ at 70 °C. (b,c) Low and high magnifications, respectively, of Au nanowires prepared with 0.5 mM $HAuCl_4$. (d) Corresponding XRD patterns of samples prepared with different amounts of CMC. See details in text.

or nanowire formation. Thus, the contrasting difference in the shape, size, and arrangement of Au morphologies produced in the presence of DEAE-D and CMC can simply be related to an entirely different course of the reaction mechanism, which we will discuss in the Discussion section.

DISCUSSION

Mechanism. The above results explain that DEAE-D can very well be employed for the synthesis of desired morphologies of Au NPs. For example, large plate like morphologies can be obtained when DEAE-D is used in a simple one-step reaction, while the S-G method helps in achieving predominantly facets or roughly spherical small NPs without the formation of nanoplates. A remarkable difference in the shape-controlling behaviors of DEAE-D and CMC can primarily be related to the presence and absence of quaternary amine functional groups, respectively. Both polymers initiate the reduction of Au(III) to Au(0) mainly due to ether oxygens (Figure 11a,f) and generate nucleating centers (Figure 11b,g); therefore, the difference in their stabilizing behaviors mainly governs the overall shape and size of the final Au morphologies. DEAE-D produces nucleating centers through stable LMCT, whereas CMC produces them without this. LMCT forms by the charge donation of ether oxygens to the electropositive metal center of $AuCl_4^-$ ions when they come in their vicinity due to electrostatic interactions with quaternary amine groups. This decreases the possibility of an instant reduction of Au(III) into Au(0) and producing nucleating centers only through LMCT. In other words, DEAE-D en routes the nucleation through a restricted number of nucleating centers, which further accommodates the rest of the Au to produce large microplates as depicted in the UV−visible behavior (Figure 3b,c). Contrary to this, an instant reduction without going through LMCT by CMC generates several nucleating centers that later grow into polyhedral morphologies as demonstrated by Figure 3e. Finally, the mode of surface adsorption of individual polymers matter and directs crystal growth in a particular direction.

DEAE-D instantaneously blocks the high energy {111} crystal planes of small nucleating centers due to its polycationic nature that leaves low energy {110}/{100} planes for participation in the growth process (Figure 11c,d). Several factors contribute to this preferential adsorption. Surface reconstruction is the most important factor among them.[51,52] The upper most layer of the atoms on a particular crystal plane is highly thermodynamically unstable because it is balanced only from one side of the plane. This is true for all crystal planes of fcc geometry but is more complex and energetically unfavorable in the case of {111} rather than {110}/{100} due to its greater atomic density, which continuously tries to attain equilibrium because of strains and energetic reasons. Under such circumstances, the growth process proceeds in the direction that allows it to attain a lower total energy. Adsorption of DEAE-D on {111} crystal planes effectively reduces the surface-free energy through electrostatic as well as van der Waals interactions and completely passivates it. Structural factors of DEAE-D further participate in the effective passivation due to the polyelectrolyte nature that allows DEAE-D to attain a rigid and expanded state best suited for complete surface coverage. This promotes nucleation on {110}/{100} planes of already created nucleating centers (as observed in Figure 3b,c) or seeds (Figure 4c,d) rather producing new nucleating centers that simultaneously expand {111} surfaces that are rapidly passivated by the

dx.doi.org/10.1021/sc400159x | ACS Sustainable Chem. Eng. 2013, 1, 1417−1431

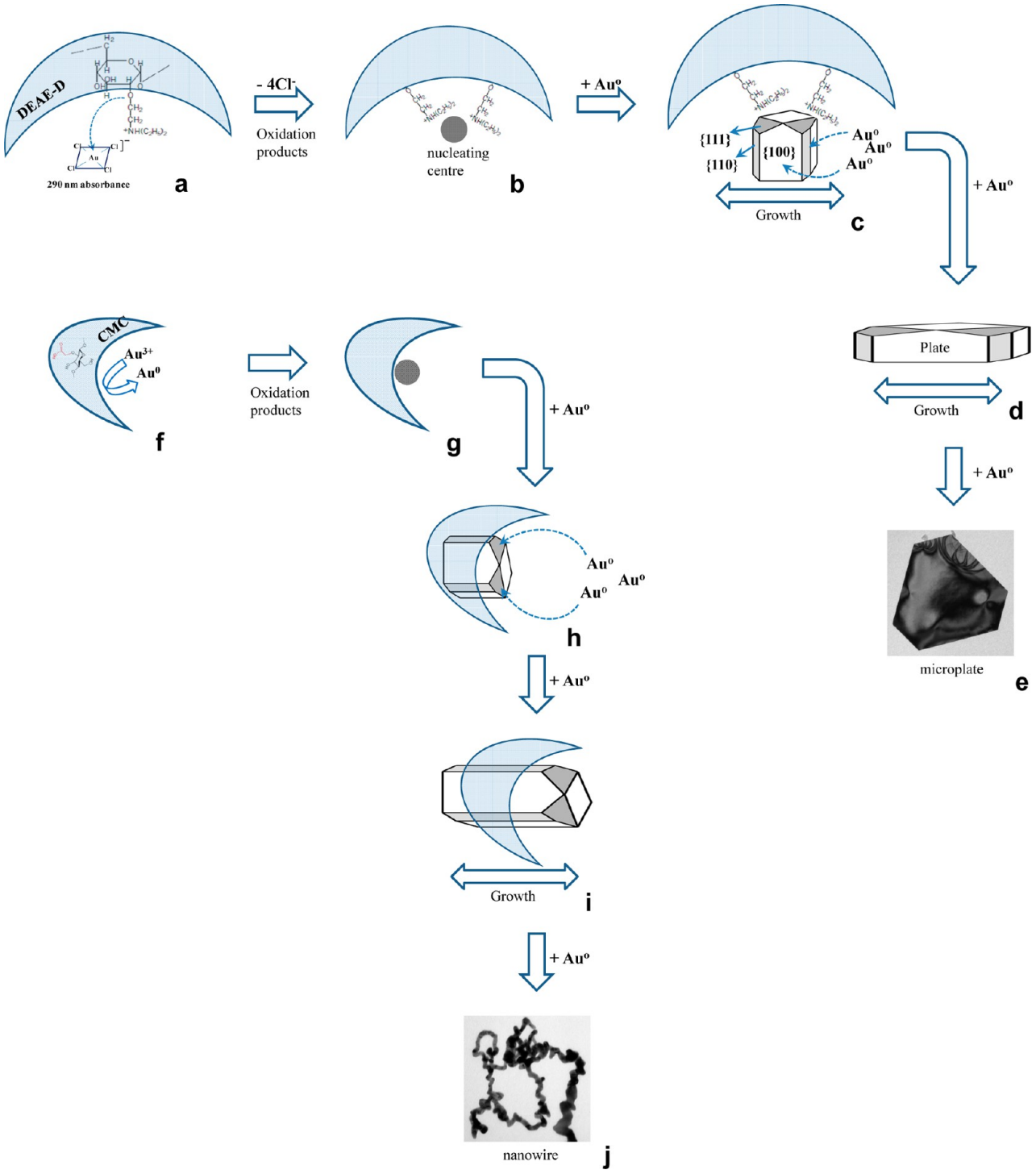

Figure 11. Schematic representation of the various steps involved in the synthesis of Au microplates (a–e) and nanowires (f–j) in the presence of DEAE-D and CMC, respectively. Steps (a) and (f) represent the reduction reaction, (b) and (g) nucleation, and (c–e) and (h – j) growth processes of respective cases. See details in text.

adsorption of fresh DEAE-D. This process continues until the precursor supply goes on and takes about 330 min to complete when 1 mM of $HAuCl_4$ is used (Figure 3d) and hence leads to the formation of large plates bound with thin edges of {110}/{100} crystal planes. The lateral planes of large plates are now actively involved in the nucleation, which is clearly evident from the wavy margins (Figure 5e, see empty block arrows); therefore, they merge with each other (Figure 5d,e, solid white arrows) to lower the overall surface energy and lead to the formation of microplates (Figure 11e). This is why all reactions generate mainly microplates whether we use 0.25 mM or 1 mM $HAuCl_4$, because once the nucleating centers are created within 15 min of the reaction (Figure 3b,c), they are directed into plate-like morphologies by DEAE-D. However, an almost similar situation exists when 7 μL of the seed is used (Figure 4c,d), but 50 μL of seed almost eliminates the possibility of microplate formation because no peak 2 appears for this reaction in Figure 4c. This is because the total amount of gold salt is

dx.doi.org/10.1021/sc400159x | ACS Sustainable Chem. Eng. 2013, 1, 1417–1431

distributed now over a large number of seeds thereby reducing the possibility of substantial growth to generate microplates.

On the other hand, a lack of quaternary amine functional groups devoid of CMC from controlled nucleation thereby produce nucleating centers proportional to the overall reduction potential of the polymer. In such a situation, the growth is solely controlled by the capping and stabilizing behavior of CMC, which prefers to adsorb on low energy {110}/{100} crystal planes due to its polyanionic nature just like that of any other anionic or neutral amphiphilic molecule leaving {111} for active participation in the growth process.[53−55] This behavior alters the direction of the growth process from that of DEAE-D and is destined for the formation of polyhedral morphologies (Figure 11g) predominantly bound with {111} crystal planes (Figure 10a), which later convert into nanowires (Figure 11i,j) as the amount of gold salt increases. Thus, polymer functionality and polyelectrolyte behavior are the most important characteristic features that simultaneously work in DEAE-D to control crystal growth.

Hemolysis. The DEAE-D-coated NPs thus produced are further subjected to hemolysis to broaden their applicability in the field of bionanotechnology. Usually, uncoated NPs are highly toxic and show strong hemolysis when their surface interacts with the cell membrane of red blood cells (RBCs).[43,56−59] The NP surface charge is the most important parameter in deciding the extent of hemolysis. We employ microplates of Figure 5 and 6, as well as core−shell NPs of Figure 8 for hemolysis, and the results are presented in Figure 12a

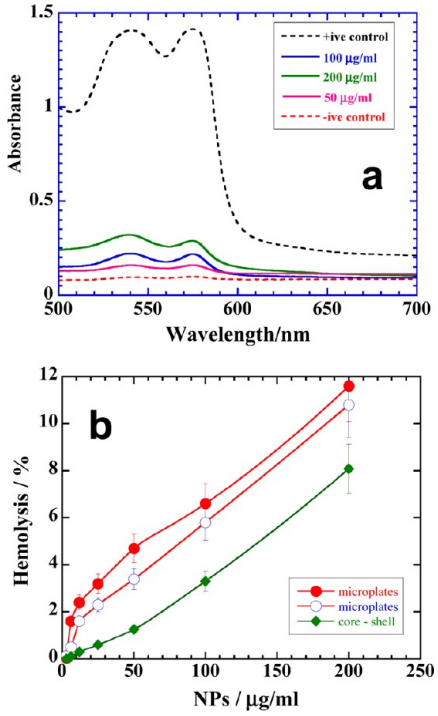

Figure 12. (a) UV−visible absorbance of hemoglobin due to hemolysis of a few concentrations of a microplate sample of Figure 5 along with positive and negative controls. (b) Percentage hemolysis induced by microplates of samples of Figure 5 (filled circles), Figure 6 (empty circles), and Figure 8 (filled diamonds).

and b. Both samples of microplates show hemolysis, which increases with an increase in the amount of sample, whereas a little hemolysis is observed for the core−shell-type NPs initially, which becomes only prominent with 25 µg/mL of the sample. Overall, microplates induce a much greater extent of hemolysis in comparison to core−shell NPs. Thus, a lower degree of hemolysis in the latter case can be attributed to an effective coating by a thick layer of DEAE-D that prevents the RBCs membrane deformation or penetration. In contrast, a much larger size of microplates provides sufficient surface area for RBCs to interact with the gold surface with a greater possibility of hemolysis. A free metal surface is considered to interact with the RBC membrane through specific interactions that are effectively screened by DEAE-D coating in core−shell NPs thereby leading to a less degree of hemolysis. These findings are quite interesting in view of intravenous drug delivery applications of DEAE-D-coated NPs where they exhibit lower affinity for RBCs and could prove to be better vehicles for drug release. This is especially important because DEAE-D is frequently used as adjuvant in vaccines and gene therapy;[7,8,11] therefore, DEAE-D-coated NPs might provide better advantages to carry a load of a specific drug for the target delivery.

CONCLUSIONS

Results conclude that biopolymeric species with specific functionality and effective surface adsorption behavior can be employed for a precise, shape-controlled, environmentally benign synthesis of Au NPs with important implications in nanotechnology. DEAE-D possesses these properties due to quaternary amine functionality and polycationic behavior and thus effectively uses them in shape-controlled synthesis of Au NPs. Quaternary amine groups attract precursor gold ions due to electrostatic interactions and supply them to reducing sites on polymer chains that control their nucleation and subsequent growth by effective surface passivation. CMC simply lacks this specific functionality and hence cannot control nucleation, while its polyanionic nature is not that effective in surface passivation of Au NPs to generate shape-controlled morphologies. This has been tested and authenticated by using two different reaction protocols in which the present polymers are involved in the direct reduction reaction and S-G method. DEAE-D thus produces extraordinarily thin large microplates and core−shell NPs that have been tested for hemolysis in view of their biomedical applications. Core−shell NPs with a thick DEAE-D coating are considered to be the best candidates for the drug release vehicles in systemic circulation in view of their little interactions with RBCs that further expands the applications of industrial important DEAE-D in bionanotechnology.

ASSOCIATED CONTENT

Supporting Information

UV−visible spectra, sample photos, and TEM images. This material is available free of charge via the Internet at http://pubs.acs.org.

AUTHOR INFORMATION

Corresponding Author

*E-mail: ms_bakshi@yahoo.com (M.S.B.), virgo16sep2005@gmail.com (P.K.).

Notes

The authors declare no competing financial interest.

ACKNOWLEDGMENTS

These studies are partially supported by financial assistance from CSIR [ref no: 01(2683)/12] and DST [ref no: SERB/F/

0328/2012-13], New Delhi. P.K. acknowledges the TEM studies done by SAIF Lab, Nehu, Shillong. G.K. thankfully acknowledges the financial support provided by the Research and Development Council (RDC) of Newfoundland and Labrador, NSERC, and the Office of Applied Research at CNA.

REFERENCES

(1) Thomas, J. J.; Rekha, M. R.; Sharma, C. P. Unraveling the intracellular efficacy of dextran−histidine polycation as an efficient nonviral gene delivery system. *Mol.Pharmaceutics* **2011**, *9*, 121−134.
(2) Yoo, S. H.; Lee, K. H.; Lee, J. S.; Cha, J.; Park, C. S.; Lee, H. G. Physicochemical properties and biological activities of DEAE-derivatized *Sphingomonas* Gellan. *J. Agric. Food Chem.* **2005**, *53*, 6235−6239.
(3) Arnold, S. M.; Fessler, L. I.; Fessler, J. H.; Kaufman, R. J. Two homologues encoding human UDP-glucose:glycoprotein glucosyltransferase differ in mRNA expression and enzymatic activity. *Biochemistry* **2000**, *39*, 2149−2163.
(4) Raksakulthai, R.; Haard, N. F. Purification and characterization of a carboxypeptidase from squid hepatopancreas (*Illex illecebrosus*). *J. Agric. Food Chem.* **2001**, *49*, 5019−5030.
(5) Dorsey, J. G.; Cooper, W. T.; Siles, B. A.; Foley, J. P.; Barth, H. G. Liquid chromatography: Theory and methodology. *Anal. Chem.* **1998**, *70*, 591R−644R.
(6) Larive, C. K.; Lunte, S. M.; Zhong, M.; Perkins, M. D.; Wilson, G. S.; Gokulrangan, G.; Williams, T.; Afroz, F.; Schoneich, C.; Derrick, T. S.; Middaugh, C. R.; Bogdanowich-Knipp, S. Separation and analysis of peptides and proteins. *Anal. Chem.* **1999**, *71*, 389R−423R.
(7) Westbrook, S. I.; McDowell, G.H . Immunization of lambs against somatotropin release inhibiting factor to improve productivity: Comparison of adjuvants. *Aust. J. Agric. Res.* **1994**, *45*, 1693−1700.
(8) Joo, I.; Emod, J. Adjuvant effect of DEAE-dextran on cholera vaccines. *Vaccine* **1988**, *6*, 233−237.
(9) Fox, R. M.; Mynderse, J. F.; Goulian, M. Incorporation of deoxynucleotides into DNA by diethylaminoethyldextran-treated lymphocytes. *Biochemistry* **1977**, *16*, 4470−4477.
(10) Rigby, P. Prologation of surivival of tumour-bearing animals by transfer of immune RNA with DEAE-dextran. *Nature* **1969**, *221*, 968.
(11) Liptay, S.; Weidenbach, H.; Adler, G.; Schmid, R. M. Colon epithelium can be transiently transfected with liposomes, calcium phosphate precipitation and DEAE dextran in vivo. *Digestion* **1998**, *59*, 142−147.
(12) Gavalas, V. G.; Chaniotakis, N. A. Polyelectrolyte stabilized oxidase based biosensors: Effect of diethylaminoethyl-dextran on the stabilization of glucose and lactate oxidases into porous conductive carbon. *Anal. Chim. Acta* **2000**, *404*, 67−73.
(13) Ghimici, L.; Constantin, M.; Fundueanu, G. Novel biodegradable flocculanting agents based on pullulan. *J. Hazard. Mater.* **2010**, *181*, 351−358.
(14) Ghimici, L.; Morariu, S.; Nichifor, M. Separation of clay suspension by ionic dextran derivatives. *Sep. Purif. Technol.* **2009**, *68*, 165−171.
(15) Bakshi, M. S.; Kaur, G.; Possmayer, F.; Petersen, N. O. Shape-controlled synthesis of PSS and PVP capped lead sulfide nanocubes, bars, threads. *J. Phys. Chem. C* **2008**, *112*, 4948−4953.
(16) Khullar, P.; Singh, V.; Mahal, A.; Kaur, H.; Singh, V.; Banipal, T. S.; Kaur, G.; Bakshi, M. S. Tuning the shape and size of gold nanoparticles with triblock polymer micelle structure transitions and environments. *J. Phys. Chem. C* **2011**, *115*, 10442−10454.
(17) Khullar, P.; Mahal, A.; Singh, V.; Banipal, T. S.; Kaur, G.; Bakshi, M. S. How PEO-PPO-PEO triblock polymer micelles control the synthesis of gold nanoparticles: Temperature and hydrophobic effects. *Langmuir* **2010**, *26*, 11363−11371.
(18) Bakshi, M. S.; Kaur, H.; Khullar, P.; Banipal, T. S.; Kaur, G.; Singh, N. Protein films of bovine serum albumen conjugated gold nanoparticles: A synthetic route from bioconjugated nanoparticles to biodegradable proteins films. *J. Phys. Chem. C* **2011**, *115*, 2982−2992.
(19) Bakshi, M. S. Nanoshape control tendency of phospholipids and proteins: Protein nanoparticles composites, seeding, self aggregation and their applications in bionanotechnology and nanotoxicology. *J. Phys. Chem. C* **2011**, *115*, 13947−13960.
(20) Bakshi, M. S.; Kaur, H.; Banipal, T. S.; Singh, N.; Kaur, G. Biomineralization of gold nanoparticles by lysozymes and cytochrome c and their applications in the protein films formation. *Langmuir* **2010**, *26*, 13535−13544.
(21) Thakor, A. S.; Jokerst, J.; Zavaleta, C.; Massoud, T. F.; Gambhir, S. S. Gold nanoparticles: A revival in precious metal administration to patients. *Nano Lett.* **2011**, *11*, 4029−4036.
(22) Pazos-Pérez, N.; Baranov, D.; Irsen, S.; Hilgendorff, M.; Liz-Marzán, L. M.; Giersig, M. Synthesis of flexiable ultrathin gold nanowires in organic media. *Langmuir* **2008**, *24*, 9855−9867.
(23) Huang, X.; Qi, X.; Huang, Y.; Li, S.; Xue, C.; Gan, C. L.; Boey, F.; Zhang, H. Photochemically controlled synthesis of anisotropic Au nanostructures: Platelet-like Au nanorods and six-star Au nanoparticles. *ACS Nano* **2010**, *4*, 6196−6202.
(24) Bakshi, M. S.; Sachar, S.; Kaur, G.; Bhandari, P.; Kaur, G.; Biesinger, M. C.; Possmayer, F.; Petersen, N. O. Dependence of crystal growth of gold nanoparticles on the capping behavior of surfactant at ambient condition. *Cryst. Growth Des.* **2008**, *8*, 1713−1719.
(25) Bakshi, M. S A simple method of superlattice formation: Step-by-step evaluation of crystal growth of gold nanoparticles through seed-growth method. *Langmuir* **2009**, *25*, 12697−12705.
(26) Laudenslager, M. J.; Schiffman, J. D.; Schauer, C. L. Carboxymethyl chitosan as a matrix material for platinum, gold, and silver nanoparticles. *Biomacromolecules* **2008**, *9*, 2682−2685.
(27) Han, M. Y.; Quek, C. H. Photochemical synthesis in formamide and room-temperature coulomb staircase behavior of size-controlled gold nanoparticles. *Langmuir* **2000**, *16*, 362−367.
(28) Miyama, T.; Yonezawa, Y. Aggregation of photolytic gold nanoparticles at surface of chitosan films. *Langmuir* **2004**, *20*, 5918−5923.
(29) de Oliveira, R. J.; Brown, P.; Correia, G. B.; Rogers, S. E.; Heenan, R.; Grillo, I.; Galembeck, A.; Eastoe, J. Photoreactive surfactants: A facile and clean route to oxide and metal nanoparticles in reverse micelles. *Langmuir* **2011**, *27*, 9277−9284.
(30) Harada, M.; Kamigaito, Y. Nucleation and aggregative growth process of platinum nanoparticles studied by in Situ quick XAFS spectroscopy. *Langmuir* **2012**, *28*, 2415−2428.
(31) Harada, M.; Katagiri, E. Mechanism of silver particle formation during photoreduction using in situ time-resolved SAXS analysis. *Langmuir* **2010**, *26*, 17896−17905.
(32) Taufany, F.; Pan, C. J.; Rick, J.; Chou, H. L.; Tsai, M. C.; Hwang, B. J.; Liu, D. G.; Lee, J. F.; Tang, M. T.; Lee, Y. C.; Chen, C. I. Kinetically controlled autocatalytic chemical process for bulk production of bimetallic core−shell structured nanoparticles. *ACS Nano* **2011**, *5*, 9370−9381.
(33) Kan, C.; Zhu, X.; Wang, G. Single-crystalline gold microplates: Synthesis, characterization, and thermal stability. *J. Phys. Chem. B* **2006**, *110*, 4651−4656.
(34) Wiley, B. J.; Lipomi, D. J.; Bao, J.; Capasso, F.; Whitesides, G. M. Fabrication of surface plasmon resonators by nanoskiving single-crystalline gold microplates. *Nano Lett.* **2008**, *8*, 3023−3028.
(35) Bai, X.; Zheng, L.; Li, N.; Dong, B.; Liu, H. Synthesis and characterization of microscale gold nanoparticles using langmuir monolayers of long chain ionic liquid. *Cryst. Growth Des.* **2008**, *8*, 3840−3846.
(36) Rodrıguez-Gonzàlez, B.; Pastoriza-Santos, I.; Liz-Marzàn, L. M. Bending contours in silver nanoprisms. *J. Phys. Chem. B* **2006**, *110*, 11796−11799.
(37) Kontrec, J.; Kralj, D.; Brečević, L.; Falini, G. Influence of some polysaccharides on the production of calcium carbonate filler particles. *J. Cryst. Growth* **2008**, *310*, 4554−4560.
(38) Zhu, D.; Damodaran, S.; Lucey, J. A. Physicochemical and emulsifying properties of whey protein isolate (WPI)−dextran conjugates produced in aqueous solution. *J. Agric. Food Chem.* **2010**, *58*, 2988−2994.

(39) Nakamura, A.; Yoshida, R.; Maeda, H.; Furuta, H.; Corredig, M. Study of the role of the carbohydrate and protein moieties of soy soluble polysaccharides in their emulsifying properties. *J. Agric. Food Chem.* **2004**, *52*, 5506−5512.
(40) Rañdler, J. O.; Koltover, I.; Jamieson, A.; Salditt, T.; Safinya, C. R. Structure and interfacial aspects of self-assembled cationic lipid−DNA gene carrier complexes. *Langmuir* **1998**, *14*, 4272−4283.
(41) Levine, S.; Dube, G. P. Interaction between two hydrophobic colloidal particles, using the approximate Debye−Hückel Theory. I. General properties. *Trans. Faraday Soc.* **1939**, *35*, 1125−1140.
(42) Derjaguin, B.; Landau, L. Theory of the stability of strongly charged lyophobic sols and of the adhesion of strongly charged particles in solution of electrolytes. *Acta Phys. Chem. URSS* **1941**, *14*, 633−662.
(43) Khullar, P.; Singh, V.; Mahal, A.; Dave, P. N.; Thakur, S.; Kaur, G.; Singh, J.; Singh Kamboj, S.; Bakshi, M. S. Bovine serum albumin bioconjugated gold nanoparticles: Synthesis, hemolysis, and cytotoxicity toward Cancer Cell Lines. *J. Phys. Chem. C* **2012**, *116*, 8834−8843; *Chem. Rev.* **2008**, *108*, 4475−4482.
(44) Arias, J. L.; Fernández, M. S. Polysaccharides and proteoglycans in calcium carbonate-based biomineralization. *Chem. Rev.* **2008**, *108*, 4475−4482.
(45) Lin, G.; Lu, W.; Cui, W.; Jiang, L. A simple synthesis method for gold nano- and microplate fabrication using a tree-type multiple-amine head surfactant. *Cryst. Growth Des.* **2010**, *10*, 1118−1123.
(46) Kaur, G.; Bakshi, M. S. Non-ideal mixing of Se−Te in aqueous micellar phase for nanoalloys over the whole mole mixing range with morphology control from nanoparticles to nanoribbons. *J. Phys. Chem. C* **2010**, *114*, 143−154.
(47) Gao, J.; Bender, C. M.; Murphy, C. J. Dependence of the gold nanorod aspect ratio on the nature of the directing surfactant in aqueous solution. *Langmuir* **2003**, *19*, 9065−9070.
(48) Pazos-Pérez, N.; Gao, Y.; Hilgendorff, M.; Irsen, S.; Pérez-Juste, J.; Spasova, M.; Farle, M.; Liz-Marzán, L. M.; Giersig, M. Magnetic−noble metal nanocomposites with morphology-dependent optical response. *Chem. Mater.* **2007**, *19*, 4415−4422.
(49) Radha, B.; Kulkarni, G. U. A real time microscopy study of the growth of gaint Au microplates. *Cryst. Growth Des.* **2010**, *11*, 320−327.
(50) Bakshi, M. S.; Possmayer, F.; Petersen, N. O. Role of different phospholipids in the synthesis of pearl-necklace type gold-silver biometallic nanoparticles as bioconjugated materials. *J. Phys. Chem. C* **2007**, *111*, 14113−14124.
(51) Jaccard, C. *Physics of Snow and Ice*; Proceedings of the Internatinal Conference on Low Temperature Science; Oura, H., Ed.; Hokkaido University: Tokyo, Japan, 1967; pp 173−178.
(52) Wang, X.-Q. Phases of the Au(100) surface reconstruction. *Phys. Rev. Lett.* **1991**, *67*, 3547−3550.
(53) Yang, Y.; Ma, H.; Zhuang, J.; Wang, X. Morphology-controlled synthesis of hematite nanocrystals and their facet effects on gas-sensing properties. *Inorg.Chem.* **2011**, *50*, 10143−10151.
(54) Lyu, L. M.; Huang, M. H. Investigation of relative stability of different facets of Ag_2O nanocrystals through face-selective etching. *J. Phys. Chem. C* **2011**, *115*, 17768−17773.
(55) Kuo, C.-H.; Huang, M. H. Synthesis of branched gold nanocrystals by a seeding growth approach. *Langmuir* **2005**, *21*, 2012−2016.
(56) Lin, Y. S.; Haynes, C. L. Impacts of mesoporous silica nanoparticle size, pore ordering, and pore integrity on hemolytic activity. *J. Am. Chem. Soc.* **2010**, *132*, 4834−4842.
(57) Lin, Y. S.; Haynes, C. L. Synthesis and characterization of biocompatible and size-tunable multifunctional porous silica nanoparticles. *Chem. Mater.* **2009**, *21*, 3979−3986.
(58) Dobrovolskaia, M. A.; Clogston, J. D.; Neun, B. W.; Hall, J. B.; Patri, A. K.; McNeil, S. E. Method for analysis of nanoparticle Hemolytic properties in Vitro. *Nano Lett.* **2008**, *8*, 2180−2187.
(59) Zhao, Y.; Sun, X.; Zhang, G.; Trewyn, B. G.; Slowing, I. I.; Lin, V. S. Y. Interaction of mesoporous silica nanoparticles with human red blood cell membranes: Size and surface effects. *ACS Nano* **2011**, *5*, 1366−1375.